Princeton Plasma Physics Laboratory

Progress in Understanding
the Enhanced Petestal H-mode in NSTX

S.P. Gerhardt, J.M. Canik, R. Maingi, D. Battaglia, R.E. Bell,
W. Guttenfelder, B.P. LeBlanc, D.R. Smith, H. Yuh, S. Sabbagh

JUNE 2014

PRINCETON
PLASMA PHYSICS
LABORATORY

Princeton Plasma Physics Laboratory
Report Disclaimers

Full Legal Disclaimer

Trademark Disclaimer

PPPL Report Availability

Princeton Plasma Physics Laboratory:

http://www.pppl.gov/techreports.cfm

Office of Scientific and Technical Information (OSTI):

http://www.osti.gov/scitech/

Related Links:

U.S. Department of Energy

Office of Scientific and Technical Information

Progress in Understanding the Enhanced Pedestal H-mode in NSTX.

S. P. Gerhardt[1], J.M Canik[2], R. Maingi[1], D. Battaglia[1], R. E. Bell[1], W. Guttenfelder[1], B.P. LeBlanc[1], D. R. Smith[3], H. Yuh[4], S. Sabbagh[5]

1: Princeton Plasma Physics Laboratory, Princeton NJ, 08543 USA
2: Oak Ridge National Laboratory, Oak Ridge, TN 37830, USA
3: Dept. of Engineering Physics, U. of Wisconsin-Madison, Madison, WI 53706 USA
4: Nova Photonics, Princeton NJ, 08540, USA
5: Dept. of Applied Physics, Columbia University, New York NY, 10027 USA

Abstract

This paper describes the enhanced pedestal (EP) H-mode observed in the National Spherical Torus Experiment (NSTX). The defining characteristics of EP H-mode are given, namely i) transition after the L- to H-mode transition, ii) region of very steep ion temperature gradient, and iii) associated region of strong rotational shear. A newly observed long-pulse EP H-mode example shows quiescent behavior for as long as the heating and current drive sources are maintained. Cases are shown where the region of steep ion temperature gradient is located at the very edge, and cases where it is shifted up to 10 cm inward from the plasma edge; these cases are united by a common dependence of the ion temperature gradient on the toroidal rotation frequency shear. EP H-mode examples have been observed across a wide range of q_{95} and pedestal collisionality. No strong changes in the fluctuation amplitudes have been observed following the EP H-mode transition, and transport analysis indicates that the ion thermal transport is comparable to or less than anticipated from a simple neoclassical transport model. Cases are shown where EP H-modes were reliably generated, though these low-q_{95} examples were difficult to sustain. A case where an externally triggered ELM precipitates the transition to EP H-mode is also shown, though an initial experiment designed to trigger EP H-modes in this fashion was unsuccessful.

7 Sections + 1 Appendix
19 Figures
101 References

Table of Contents

Note: table of contents for referee convenience. It need not be in the published article.

1. Introduction

1.1 Motivation

The spherical torus [1] has the potential to provide the fusion core for a number of next-step fusion missions. These include devices to prototype nuclear technologies for DEMO [2-6], fusion pilot plants [7], and full fusion reactors [8,9]. These studies often invoke a level of energy confinement well beyond that projected by the ITER-98(y,2) scaling expression [10]. For instance, a recent pilot plant study [7] found that a confinement level specified by $H_{98(y,2)}$=1.3-1.35 was desirable, while the reactor study in Ref. [9] specified $H_{98(y,2)}$=1.6. The component test facility (CTF [11]) and fusion nuclear science (FNSF) facilities described in Refs. [2-4,6] all assume $1.3 < H_{98(y,2)} < 2.1$.

Spherical torus H-mode thermal confinement [12] with boronized plasma facing components has shown scalings with I_P and B_T [13-15] that are significantly different from the ITER-98(y,2) expectation. For instance, from Ref. [13], the I_P exponent is typically in the range of 0.5-0.6, compared to the ITER-98(y,2) exponent of 0.93. The toroidal field exponent has been found to be ~0.8-1.1, compared to 0.15 in the ITER98(y,2) expression. However, numerical values of the confinement time are roughly similar to the values from that conventional aspect ratio scaling expression. Furthermore, lithium conditioned H-mode scenarios in NSTX showed confinement not significantly different in magnitude and scaling from the ITER-98 expression, though $H_{98(y,2)}$ multipliers up to 1.3 [16] have been observed with strong lithium conditioning of the PFCs [17,18] (note that the confinement in NSTX has generally been observed to increase with the level of Lithium conditioning [19,20]). Hence, while H-mode thermal confinement values in the ST can be comparable to that in conventional aspect ratio devices, reliable access to the confinement regimes anticipated for next-step devices is not assured.

Various regimes with enhanced confinement compared to H-mode have been observed in conventional aspect ratio tokamaks. For instance, internal transport barrier plasmas [21] can have substantially higher levels of stored energy than comparable L-mode discharges. Enhanced edge transport barriers have also been observed in the form of the VH-mode [22-28]. Both of these regimes have produced confinement multipliers $H_{98(y,2)}$ approaching or exceeding two. Internal transport barrier regimes have been accessed in NSTX [29,30] with HHFW heating [31], though the L-mode edge results in reduced global confinement and undesirable stability properties. While the VH-mode itself has never been observed in a spherical torus, a different regime of enhanced confinement at the plasma edge has been observed. It is the purpose of this paper to discuss this regime, known as the Enhanced Pedestal H-mode, or EP H-mode.

1.2 Definition of the Enhanced Pedestal (EP) H-mode.

The enhanced pedestal (EP) H-mode [32,33] is an enhanced confinement regime in NSTX characterized by the following features:

- There is a transition to the EP H-mode from the normal H-mode phase. Transitions from L-mode directly to EP H-mode have not been observed. This transition to EP H-mode is typically triggered by some external event such as an ELM.

- There is a region towards the edge of the plasma where the ion temperature gradient is much steeper than in standard H-mode. This is illustrated most clearly in Fig. 1, where the maximum absolute value of the T_i gradient at the outboard midplane is plotted as a function of plasma current. This maximum gradient is determined by fitting a line to sets of four adjacent CHERS channels, with the error bars determined by the uncertainty in the fit parameters given the uncertainties in the individual T_i measurements. This process is repeated across varying sets of four channels across the plasma edge to determine the largest local gradient. The blue points are taken from the EP H-mode phase of the discharge, and show substantially higher T_i gradients than in the H-mode phases in red.

- The region of steep T_i gradient coexists spatially with a region of strong rotation shear. There is often a local minima in the rotation in this region, though that is not a strict requirement for the identification of the regime.
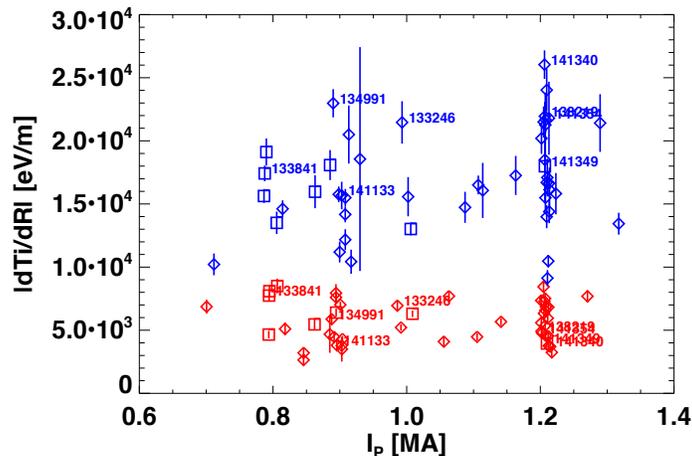

Fig. 1: Maximum ion temperature gradient for EP H-mode (blue) and H-mode (red) examples in NSTX. The difference between squares and diamond symbols will be described in Section 3. The database analysis that produced this plot will be described in more detail in Section 4. The discharge numbers refer to discharges that will be discussed in detail in this paper.

1.3 Overview of this paper

This paper provides an overview of EP H-mode observations from NSTX. Section 2 provides additional general characteristics of the EP H-mode, while section 3 describes the typical profile shapes and evolution. Section 4 presents database analysis of EP H-mode examples in NSTX. Section 5 describes measurements of turbulent fluctuations and transport analysis. Section 6 describes attempts to control the EP H-mode transition and subsequent evolution, while Section 7 provides some conclusions.

1.4 Description of the NSTX Device

NSTX [34] is a medium sized spherical torus device located at Princeton Plasma Physics Laboratory. Plasmas typically have a major radius of 0.9 m, and a minor radius of 0.6 m. Toroidal fields strengths for typical discharges are in the range $0.35 < B_T$ [T] < 0.55, with typical plasma currents for H-mode discharges in the range of $600 < I_P$ [kA] < 1200. All plasmas described in this paper are heated by neutral beam injection in the direction parallel to I_P, with up to 7 MW available [35]. High Harmonic Fast Wave (HHFW) heating is also available [31], though it was not utilized for these plasmas.

NSTX plasmas are assessed with a comprehensive set of diagnostics. The electron temperature and density profiles are measured with a multi-pulse Thomson scattering (MPTS) diagnostic [36]. The impurity ion (C^{6+}) temperature, density, and toroidal rotation are measured by a charge exchange recombination spectroscopy (CHERS) system [37], with an averaging time of 10 ms per sample. Note that both of these systems are located at the vessel midplane, which is quite close to the plasma midplane for most of the plasmas discussed in this paper. The magnetic field pitch angle is measured with a motional Stark effect (MSE) polarimetery system [38], and, when available, is used to constrain equilibrium reconstructions with the LRDFIT code [39] on a case-by-case basis. Routine MHD equilibrium reconstructions with the NSTX implementation [40,41] of the EFIT code [42] are also available and used in this analysis; note that these routine post-shot reconstructions are not constrained by MSE measurements.

2. General Characteristics of EP H-mode

The temporal characteristics of EP H-modes in NSTX can roughly be divided into two groups. The first group contains high-current cases which transition to this confinement regime at the end of the I_P ramp or early in the I_P flat-top. The current profile is typically rapidly evolving in these cases, and the EP H-mode phase is typically of limited duration due to disruptions or transition back to H-mode. The second group contains cases that transition to EP H-mode much later in the I_p flat top. These cases have demonstrated the highest confinement and longest pulse of all EP H-mode examples observed to date.

2.1 Examples of the Early Transition EP H-modes

The first EP H-mode plasmas observed in NSTX had comparatively short durations of the steep ion-temperature gradient [32], and were typically observed early in the discharge in higher-current plasmas. Two examples of this sort of discharge are shown in Fig. 2. The quantities illustrated are indicated in the figure caption, with some clarification required for the stored energy traces in Fig. 2c). The solid line in that frame corresponds to the stored energy calculated from the MHD equilibrium reconstruction with the LRDFIT code, while the dashed lines are from interpretive TRANSP [43] simulations. The stored energy in this simulation is the sum of the thermal energy (indicated in the dotted line) and the fast ion stored energy, as computed by NUBEAM [44].
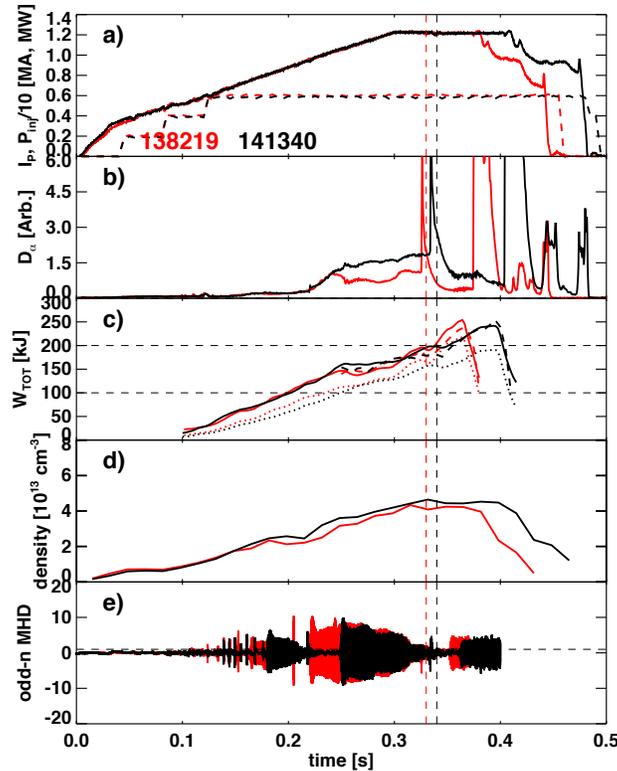
Fig. 2 *Time evolution of short-lived EP H-mode example discharges. Shown are a) the plasma current and beam power, b) the divertor D_α emission, c) the stored energy, d) the line averaged density, and e) the odd-n MHD trace, indicative of n=1 rotating kink/tearing modes.*

In these examples, which came from two different run campaigns, the plasma current ramps to I_P=1200 kA, with the full 6 MW of neutral beam heating power applied by the time the current has reached 700 kA. The plasmas transition to H-mode at t=0.13 s (141340) and t=0.15 s (138219). A large ELM then occurs (see Fig. 2b)), which triggers the transition to EP H-mode. This transition is indicated by the

dashed vertical lines in all frames. The stored energies then begin to ramp, with the dominant effect being an increase in the thermal stored energy. As will be shown in Section 3, there is a remarkable steepening of the edge ion temperature gradient during the EP H-mode phase. In these cases, the line-average density stays approximately fixed during the EP H-mode phase. In both cases, a disruption ends the EP H-mode phase, presumably due to the large pressure gradient, however, macrostability calculations for these plasmas have not been systematically attempted.

Examples like these indicate the potential value of the EP H-mode configuration. However, discharges with longer durations are clearly required in order to understand the potential of the regime. The next section discusses discharges of this type.

2.2 Examples of the Late-Transition EP H-modes

Two examples of more stationary, late-transition EP H-modes are described in this section. Here, the phrase late-transition refers to cases where the transition occurs well after the current ramp is complete. Time traces from these discharges are shown in Fig. 3, where the individual frames are largely similar to that in Fig. 2. The most significant difference is in frame e), which shows the current in one of the radial field coils. The more rapid dynamics in this coil are typically driven by the shape and vertical position control feedback loops; the significance of this waveform will be made apparent in later discussion. Fig. 4 illustrates the boundary shapes for these two discharges during their EP H-mode phases.

Discharge 134991 was described in Ref. [33], and represented the longest-duration EP H-mode discharge at the time. This 900 kA discharge from the 2009 campaign was made during an experiment to develop scenarios for experiments with the Liquid Lithium Divertor (LLD) [45] in 2010. As part of this development effort, strike-point controllers [46,47] were being developed, and super sonic gas injection [48] was being used to supplement the standard low-field and high-field side [49] fuelling. A large ELM at t=0.555 seconds triggers the transition to EP H-mode. This results in an increase in the global confinement, with the stored energy ramping from ~210 kJ to ~320 kJ. This high performance phase lasts approximately 300 ms, or 2-3 confinement times, before a disruption occurs.

The second discharge in the figure (141133) was observed as part of the database study reported in Section 4. As can be seen in Fig. 4, this is a high-elongation and triangularity discharge typical of the highest performance NSTX discharges [15,50], without feedback control of the strikepoints. In this case, a small ELM at t=0.5 s triggers an apparent transition to EP H-mode. A second ELM occurs at t=0.65 s, leading to a large stored energy loss. However, the plasma recovers into EP H-mode once more. The stored energy ramps to ~230 kJ, corresponding to $H_{98(y,2)} \sim 1.5$. The density ramps throughout the EP H-mode phase in both this and the other discharge in the figure. In both cases, this is due to the accumulation of carbon in the

discharge; the deuteron inventory is well regulated, as is typical of discharges with significant lithium conditioning of the PFCs [51]. This discharge is extremely quiescent during the EP H-mode phase, showing no significant dynamics until the heating power is turned off at 1.2 seconds and the current rampdown is initiated at 1.25 s.

The current in the radial field coil (frame e) is shown as a measure of the global quiescence of the discharge. This current is determined entirely by feedback loops for the plasma elongation and vertical position [52]. In particular, discharge 141133 shows almost no variation in this current, indicating that the configuration is quite steady and free of transients; this level of variation is lower than in typical H-mode discharges, or in discharge 134991 (though it should be noted that the poorly tuned strike-point controllers likely also played a role in the radial field variations in that discharge).
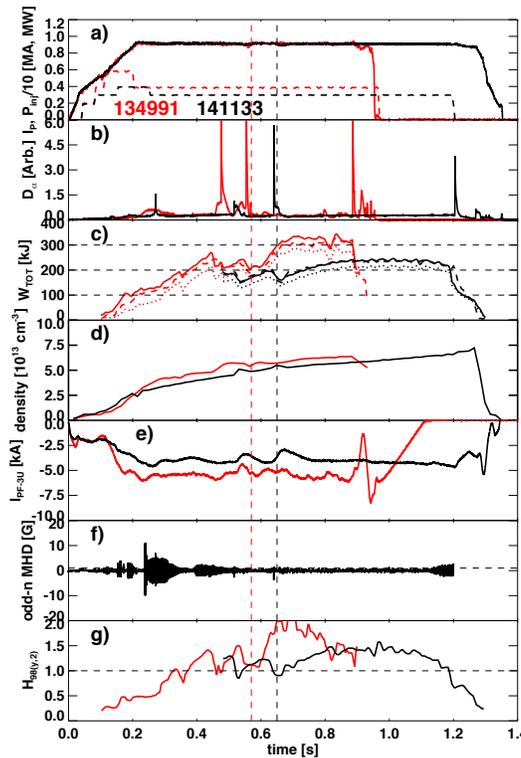
Fig. 3: Time evolution of long-pulse EP H-mode example discharges. Shown are a) the plasma current and injected neutral beam power, b) the divertor D_α emission, c) the stored energy, d) the line-average density, e) the current in the radial field coil, f) the odd-n rotating MHD signal (141133 only), and g) the $H_{98(y,2)}$ confinement multiplier. See text for additional details.

3. Profile Variations in EP H-mode

3.1 Overview of the Edge Pedestal Characteristics in EP H-mode

As first described in Refs. [32,33], the EP H-mode phase is characterized by a steep gradient in the ion temperature profile at the edge of the plasma. However, more recent examination of the NSTX database has shown that the exact location of the steep gradient region with respect to the separatrix can vary significantly. This is illustrated in Fig. 5, where the profiles from three different discharges are plotted in three columns. These profiles are plotted against major radius, so that complications associated with flux-mappings can be avoided. The separatrix location is shown as the gray shaded region for all figures, determined by the values give by equilibrium reconstruction, the T_e=40 eV location, and the T_e=80 eV location.
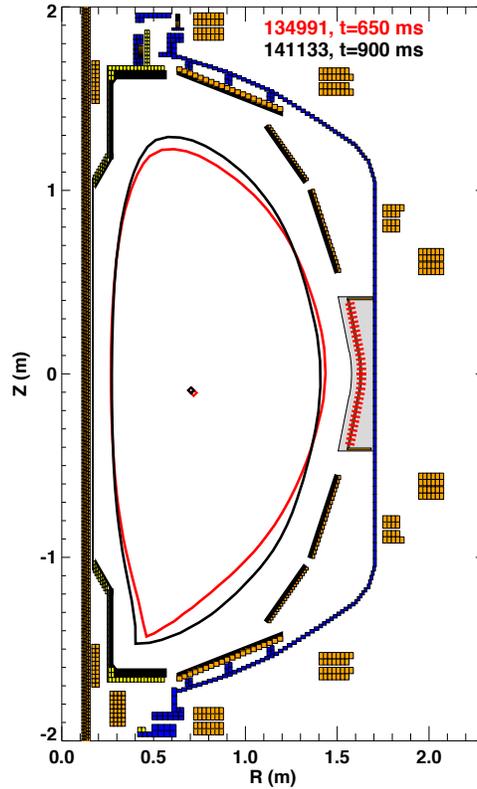
Fig. 4: Typical separatrix shapes for the long-pulse EP H-mode examples in Fig. 3.

In this figure, the top row shows the electron and ion temperatures, along with both tanh fits to T_i and a line tangent to the point of the maximum T_i gradient. The tanh fit in this and other figures is defined via the function:

$$Y(X) = Y_{offset} + \frac{\left(Y_{pedestal} - Y_{offset}\right)\left(1 + 0.5\alpha_{slope}z\right)}{1 + e^{-2z}}, \tag{1}$$

with $z=2(X_{symmetry}-X)/\Delta_{width}$ [53]. Here, Y can represent T_e, T_i, n_e or any other profile quantity, while X can represent either outboard midplane major radius or some flux surface label such as normalized poloidal flux. Y_{offset}, $Y_{pedestal}$, α_{slope}, $X_{symmetry}$, and Δ_{width} are fit parameters determined by a non-linear fitting routine [54].

The second row shows the toroidal rotation profile (here, indicated by the rotation frequency F_T in kHz), as well as the quantity $E_R + V_P B_T = \dfrac{1}{6eN_C}\dfrac{dP_C}{dR} + V_T B_P$. The poloidal rotation is generally small in NSTX [55], and so the $V_P B_T$ term may not be a significant contributor to this calculation; this was previously found to be the case for discharge 134991 [33]. However, because it has not been assessed across this wider range of EP H-mode cases, it is not possible to systematically neglect it with high confidence. The bottom row shows the electron and scaled carbon density profiles, along with spline fits to those profiles.
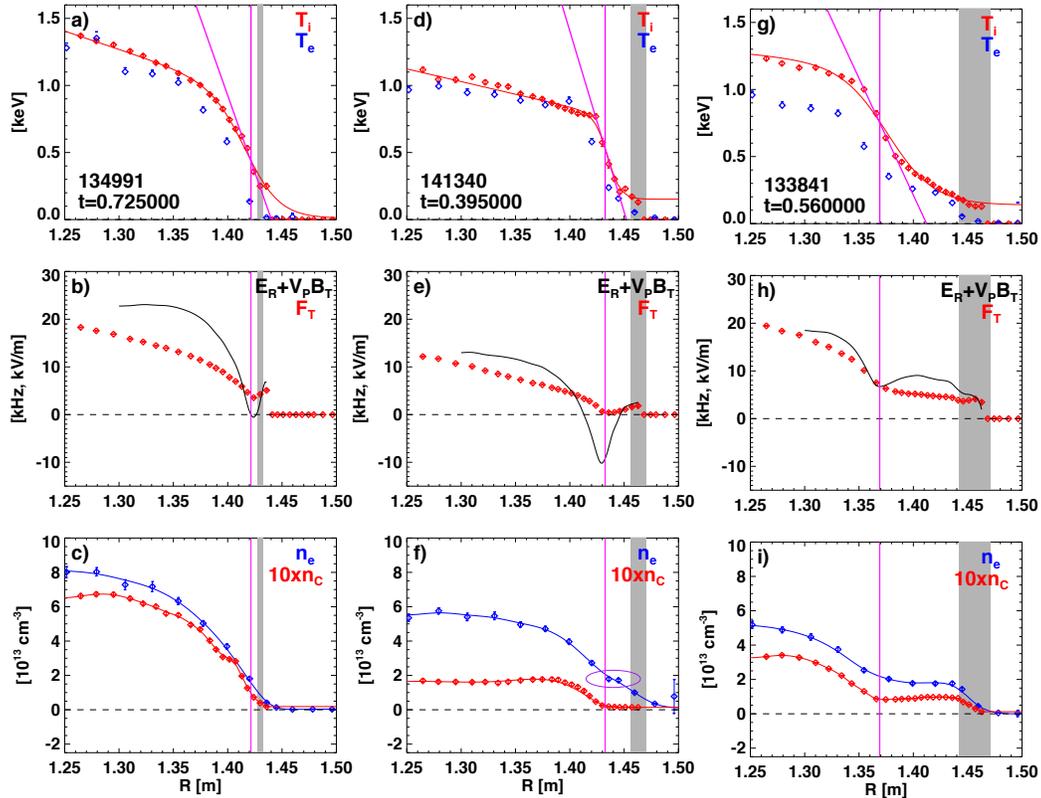
Fig. 5: Examples of profile shapes during EP H-mode in NSTX. The top frame of each column shows the ion and electron temperature profiles. The points show the data, while the lines show tanh fits, magenta lines marks the location of maximum ion temperature gradient and the tangent line to the profile at that point. The middle frames show the toroidal rotation frequency F_T and $E_R + V_P B_T$ profiles, while the bottom frames show the electron and carbon density profiles. The grey shaded regions indicate the approximate regions of the separatrix. Note that the magnetic axis is typically at R=1.03 m for these cases. See text for additional details. The circle in frame f) indicates a small local flattening of the electron density profile.

The left-most column of Fig. 5 shows the edge profiles for the long-pulse EP H-mode discharge 134991, whose time evolution is illustrated in Fig. 3. In this case, the region of steep T_i gradient is very close to the plasma edge. There is a clear minima in the rotation profile, with a deep E_R well developing. The profiles for the other long-pulse discharge in Fig. 3 (141133) are of similar shape, and will be illustrated below.

The middle column of Fig. 5 shows the profiles for a case typical of the short-lived EP H-modes that transitions before or just after the start of the I_P flat-top; see Fig. 2 for the time evolution of 0D quantities in this case. In this example, the region with the steepest T_i gradient is shifted in a few cm, with a clear region of lower T_i gradient farther outside. However, the rotation profile minima and E_R well are still present. Note that these profiles are not maintained in steady state; the disruption follows soon after the time shown in the figure.

Finally, the right most column shows a case where the steep T_i gradient is shifted inward ~10 cm from the plasma edge. There is an associated inward shift of the region of sharp rotation gradient indicating that the relationship between the steep ion temperature gradient and rotation is maintained. In this case, both T_e and n_e show a double-barrier structure, and the configuration could be called a wide radius internal transport barrier (ITB) as well as an EP H-mode. For this reason, cases such as in the right column of Fig. 5 are noted with squares in the scatter plots below and in Fig. 1, whereas cases such as in the left and center column will be denoted with diamonds.

3.2 Time evolution of the edge pedestal following the transition to EP H-mode

The data in Fig. 5 provide a clean indication of the different profile shapes in EP H-mode, but do not provide information on the time evolution to those profiles. Hence, Section 3.2 provides information about that evolution.

The profile evolution for the example in the center column of Fig. 5 (discharge 141340) is shown in Fig. 6; this is the high-current example transitioning to EP H-mode early in the discharge. The CHERS data (F_T, T_i, E_R) and MPTS data (T_e, n_e) are on slightly different time bases, so nearly synchronous samples are indicated with the same color; also recall that the CHERS data is averaged over 10 ms windows. At t=330ms, the configuration is in H-mode, with relatively broad density, temperature and rotation profiles. The bottom of the T_i pedestal is not resolved by the CHERS diagnostic for this time slice due to the low edge electron temperature, and so the E_R features at the edge are not fully resolved.

After t=340 ms, the EP H-mode transition occurs following a large ELM, with a number of associated changes in the profiles. The electron density and temperature at the plasma edge are reduced following the ELM, and the rotation immediately develops a local minima. The ion temperature at the very edge is also transiently reduced, though the core ion temperature is largely unchanged; this results in a region of sharp T_i gradient at the location where the two regions connect. These rotation and pedestal dynamics result in the formation of a deep well in the E_R profile. Indeed, both the magnitude and spatial scale of the large E_R shear region is significantly larger in the EP H-mode phase than in the H-mode phase [33].

From that point onward, the minima in the rotation remains, marked by vertical dashed lines in the figure for the later time slices. The width of the ion temperature pedestal

increases at roughly fixed gradient scale length until the EP H-mode phase ends with a disruption. Note the apparent local flattening of the density profile, barely visible in the bottom center frame of Fig. 5, but clearly visible in Fig. 6c) within the magenta oval.
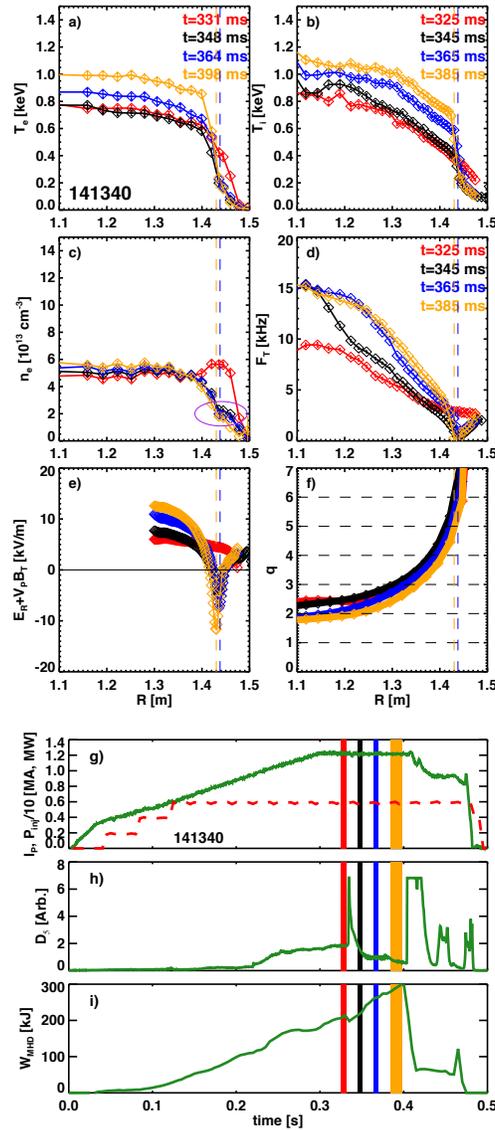
Fig. 6: Profiles and waveforms for a typical early-transition EP H-mode example 141340. The upper frames show the time evolution of the profiles of the a) electron temperature, b) ion temperature, c) electron density, d) toroidal rotation frequency, e) radial electric field (formally, $E_R+V_P B_T$), and f) safety factor (q). The bottom frames show the time evolution of the g) plasma current and heating power, h) divertor D_α, and i) total stored energy. The vertical bands in g)-h) indicate the ranges of time for the profiles plotted in a)-f). The dashed vertical lines in frames a)-f) indicate the location of the rotation minima for selected times.

It has been speculated that the minima in the rotation profile is associated with a single rational surface [33]. However, as illustrated in Fig. 6f), isolating which surface would play this role has proven difficult. This frame shows the q profile at the time of interest, with the horizontal lines indicating where a rational surface might be anticipated. The minima in the rotation appears to not be located at the q=2, 3, or 4 surfaces. It may be located at one of the q>4 surfaces, though isolating which one is essentially not possible due to the large magnetic shear. Alternatively, as discussed in Sect. 7, it is possible that 3D effects are present that render this mapping more difficult to interpret. Also note that there are some rotating n=1 MHD modes present during the EP H-mode phase; these are visible in Fig. 2e). However, these modes have decreased in amplitude by the time the EP H-mode transition occurs. Inspection of the spectrograms shows that these modes have frequencies of ~5 kHz during that phase of the discharge, which is clearly well above the frequency of the minima in the rotation, and implies that they are not directly responsible for the rotation minima.

Fig. 7 shows similar profile information, for the long-pulse quiescent EP H-mode scenario in discharge 141133 (see Fig. 3). Similar dynamics can be observed in this example, with the ELM at t=0.640 s leading to a substantial loss of the edge electron (frame a)) and ion temperatures (frame b)), as well as of the toroidal rotation frequency (frame d). In this case, it appears as if the plasma may have been in a weak EP H-mode before the ELM at t=0.51, so the E_R shear is already rather strong before that ELM. However, because the T_i gradient is closer to the edge in this case, the full gradient is not resolvable (the bottom of the T_i gradient is in a region with too low electron temperature to fully ionize carbon). No minima in the rotation frequency profile is visible during the EP H-mode phase except for the time slice at t=0.845 s, though this may be due to the limited measurement range of the CHERS diagnostic in this case. As is evident in Fig. 3f, the EP H-mode phase has no low-frequency n=1 modes until a small n=1 mode begins to grow at 1.15 s. Inspection of the complete magnetic spectrogram shows that there are no macroscopic MHD modes present during the bulk of the EP H-mode phase, indicating that large rotating magnetic islands are unlikely to play a significant role in the rotation dynamics.

Finally, Fig. 8 shows the profile evolution for the case with the region of steep T_i gradient shifted substantially inward. In this case, an ELM at t=0.415 s appears to drive the transition. As with the case in Fig. 6, that ELM results in a substantial drop in the edge ion temperature, with the perturbation in this case penetrating to R=1.37 m and leading to increased T_i gradient at that location. The ion temperature outside this radius then stays at the lower value, while the value inside the vicinity of that radius grows to much higher values than before the ELM. This case develops very clear double-barrier structures in the electron density and temperature profiles, with the n_e barriers separated by 8-10 cm (note that the minor radius is typically ~60 cm for these plasmas). There is no minimum in the toroidal rotation frequency, but rather an inflection point at the location of the steep T_i gradient. Note that this inflection point is in vicinity of the q=4 surface, though there is no indication in the rotation profile of a magnetic island at that location (the plasma maintains a rotation frequency of ~5 kHz at this location). Also note that the ELMs in this discharge were themselves triggered by impulsively applied 3D fields [56-58]. EP H-modes triggered in this fashion will be discussed in Section 6.2.

Identification of cases like in Fig. 8 with EP H-mode may appear problematic, as the steep T_i gradient region is shifted well away from the separatrix. However, the examples in this

Section show that there is a continuum of profile shapes, from those with the steep T_i region at the very edge to those with that region shifted substantially inward. Under the assumption that the underlying physics has similarities, it will be valuable to consider these cases as different manifestations of similar underlying phenomenon.
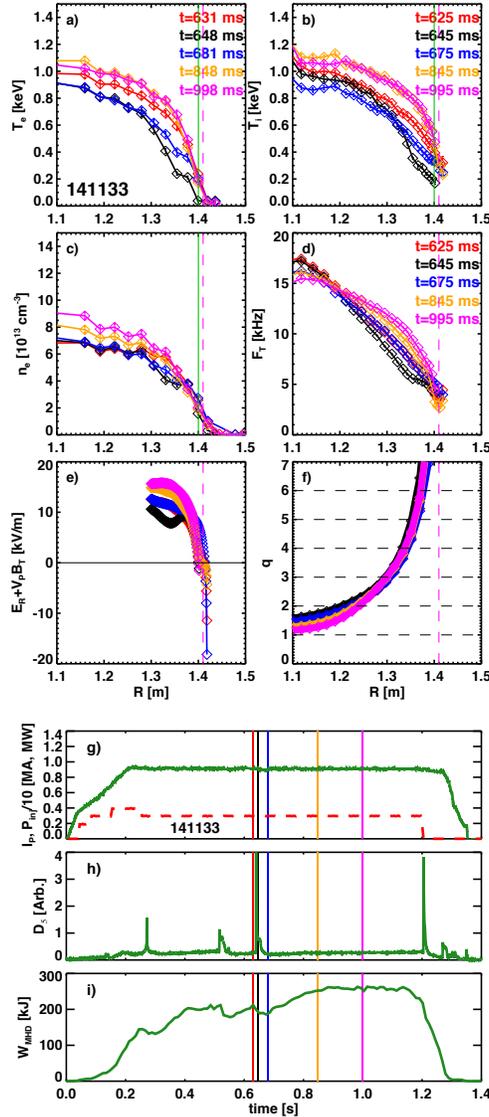
Fig. 7: Profiles and waveforms for the long-pulse quiescent EP H-mode case in Fig. 3 (141133). The frames show the same quantities as in Fig. 6. The green vertical line indicates the location of the BES measurements presented in Fig. 13.
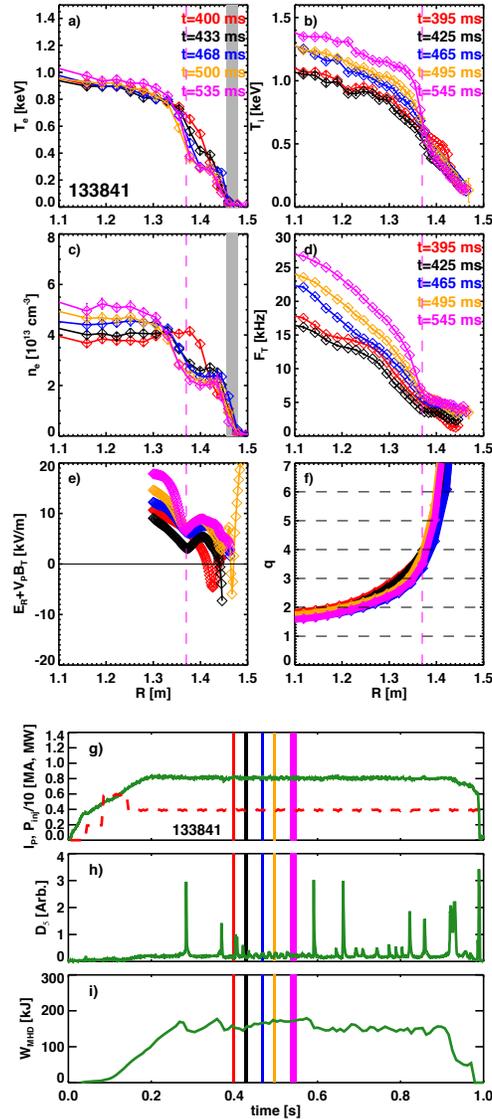
Fig. 8: Profiles and waveforms for an EP H-mode case with the region of steep ion temperature shifted inward. The frames show the same quantities as in Fig. 6.

4. Database analysis of EP H-modes

As part of this research, a significant effort was put into identifying and analyzing a database of EP H-mode examples. As a first step in this study, all NSTX discharges with particularly steep gradients in the ion temperature were identified via automated analysis. These cases were then individually examined to see if they met the characteristics of the EP H-mode, as defined in Section 1. It was this process that identified the long-pulse EP H-mode example 141133 noted in Figs. 3 and 7. These EP H-mode cases were then incorporated into a more detailed database, which yielded the analysis shown in Fig. 1 and the remainder of this section.

The detailed EP H-mode database evaluates quantities during high performance EP H-mode phase, and during the H-mode phase preceding the EP H-mode transition. Equilibrium quantities stored in the database come from reconstructions with the LRDFIT code, as well as the NSTX implementation of the EFIT code. Confinement metrics are extracted from TRANSP runs that use NUBEAM to compute the coupled neutral beam power. Consistency of these data is checked by comparing the measured and predicted neutron emission, and comparing the total stored energy computed by TRANSP (thermal+fast ion energy) and computed by the equilibrium reconstruction codes. Fits to the edge T_e and T_i pedestals as a function of major radius with the tanh function are also included in the database analysis. The TRANSP and LRDFIT runs used in this database are shown in Appendix A.
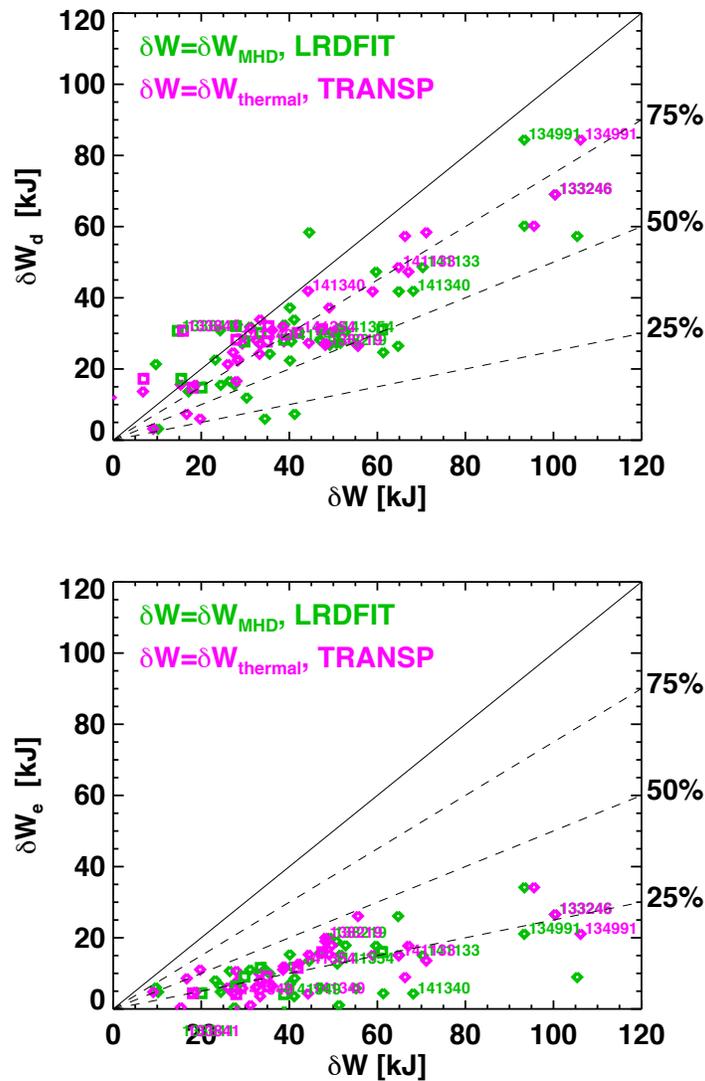
Fig 9: Increments of the deuterium (top) and electron (bottom) stored energy, as a function of the total stored energy increment δW. The green points are based on calculating δW from

4.1 Global Confinement Characteristics

As a first analysis step using this database, the increments in stored energy following the EP H-mode transition were examined to determine if, as anticipated from Sect. 3, the increase in stored energy following the EP H-mode transition is largely in the ion channel. Fig. 9 shows the increase in the total ion stored energy in frame a), and the increase in the electron stored energy in frame b), as a function of the total energy increase. The total energy increase is calculated from the MHD equilibrium reconstruction (δW_{MHD}), or from the increment of the total thermal energy as computed by TRANSP. Note that the sum of the electron and ion thermal energy increases is essentially equal to the total thermal energy increase ($\delta W_e + \delta W_d = \delta W_{thermal}$, $\delta W_{impurity}$ being small), but they are not constrained to match the increment of energy from MHD equilibrium reconstruction.

Fig. 10: Confinement multiplier as a function of q_{95} for NSTX EP H-modes. Red points correspond to the H-mode phase of the discharge before the transition to EP H-mode, while

The results of this analysis follow the expected trend. The electron energy increment is typically ~25% of the total energy increment. However, the increase of deuterium stored energy is typically 75% of the total increase. Hence, physics mechanisms that impact the ion thermal transport are anticipated to be important for determining the characteristics of the EP H-mode.
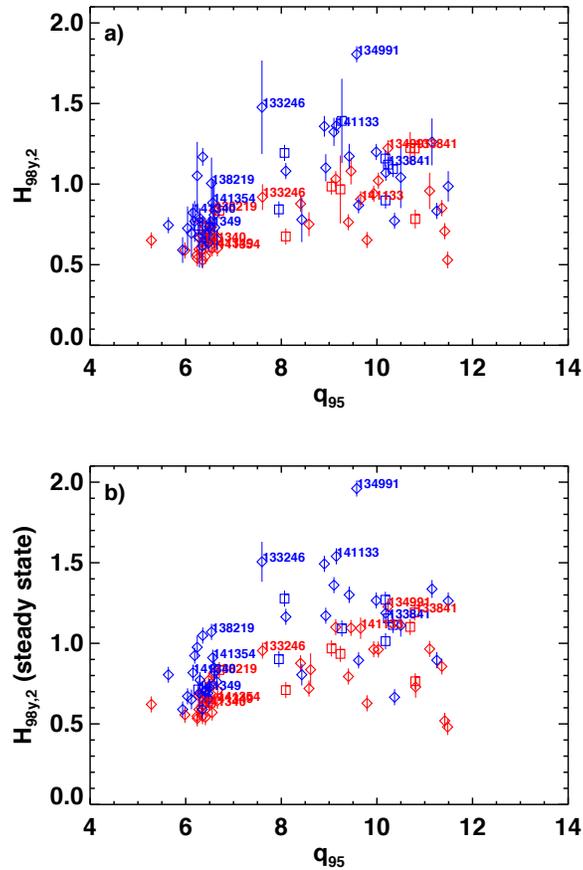
The confinement multipliers for EP H-modes and the proceeding H-mode phases are shown in Fig. 10, as a function of q$_{95}$. Here, the confinement multiplier is defined as H$_{98(y,2)}$=τ_E/$\tau_{98(y,2)}$. The confinement time is calculated in Fig 10a) as τ_E=W$_{th}$/(P$_{abs}$-dW$_{th}$/dt), with W$_{th}$ the thermal energy and P$_{abs}$ the absorbed power. This definition can yield a somewhat noisy evolution of the confinement time due to the time derivative in the denominator, and so the same calculation is shown in Fig 10b), but with the dW$_{th}$/dt term set to zero. The results are broadly similar, though with some rearrangements of the points and often smaller error bars in Fig. 10b)

The H-mode phases in these discharges tend to cluster in the range 0.8<H$_{98(y,2)}$<1.0, whereas the EP H-mode cases can have confinement multipliers in excess of H$_{98(y,2)}$=1.5. Note the large cluster of data points at q$_{95}$=6. These are the "early transition" EP H-modes, many of which come from a dedicated experiment, the results of which are discussed in Section 6. As discussed in Section 2, these cases tend to disrupt not long after the EP H-mode transition, and so do not achieve the highest levels of confinement. The higher q$_{95}$ cases often show quite high levels of confinement, aided by the fact that the EP H-mode duration can be longer in these cases. Note that EP H-mode has been observed over a large range of q$_{95}$.

Additional pedestal parameters are shown in Fig. 11. In this case, the ion temperature pedestal is fit by eqn. 1, as a function of major radius; pedestal-top ion temperatures in excess of 1 keV are achievable in EP H-mode. Note that due to the lack to T$_i$ data at the bottom of the pedestal (due to the low electron temperature), tanh fits of single time slices are typically not well constrained in H-mode. As a consequence, T$_{i,ped}$ is typically not resolvable by these fits, and so no H-mode points are shown here. However, the profiles in Figs 6-8 show that the edge ion temperatures are indeed much higher in EP H-mode than H-mode. This result can also be inferred from Fig. 1, where the maximum T$_i$ gradients are shown in H-mode and EP H-mode.

The pedestal collisionality is shown in Fig. 11b). Here, the collisionality is defined as $v_{e,ped}* = 0.012 n_{e,ped,20} Z_{eff} q_{95} R / \varepsilon^{3/2} T^2_{e,ped,keV}$. The electron density and temperature profiles are sometimes not easily fit to tanh functions. For instance, the multiple gradient region behavior shown in Figs 5-8 can confuse the simple tanh fits. Other times, the use of profile data at a single time results in poor fits (note that recent NSTX pedestal physics studies [53, 59, 60] use a sophisticated set of "kinetic efit"

reconstructions, flux mapping, and conditional averaging technique to improve the quality of the fits using multiple time slices). Hence, $T_{e,ped}$ and $n_{e,ped}$ are derived from the values of their respective profiles, at the radial location of the top of the ion temperature pedestal. In any case, the EP H-mode cases have been observed over a range of pedestal collisionalities, including cases with $\nu_{e,ped}$ significantly less than unity. Hence, unlike the NSTX type-5 ELM regime [61], the EP H-mode regime is observed to be compatible with low collisionality.

Finally, the pedestal poloidal beta ($\beta_P = 2\mu_0 P / B_P^2$) value is shown in Fig. 11c). Quite high values of this parameter have been achieved, typically in the higher-q_{95} EP H-mode examples. However, the data does not yet exist to make a systematic study of how the pressure pedestal width scales with β_P in these cases, as the single time-slice pedestal fits noted above are incapable of accurately resolving the width due to the lack of points in the pedestal region. Upgrades in the radial coverage of the Thomson scattering system for NSTX-U [62,63] should improve this situation.
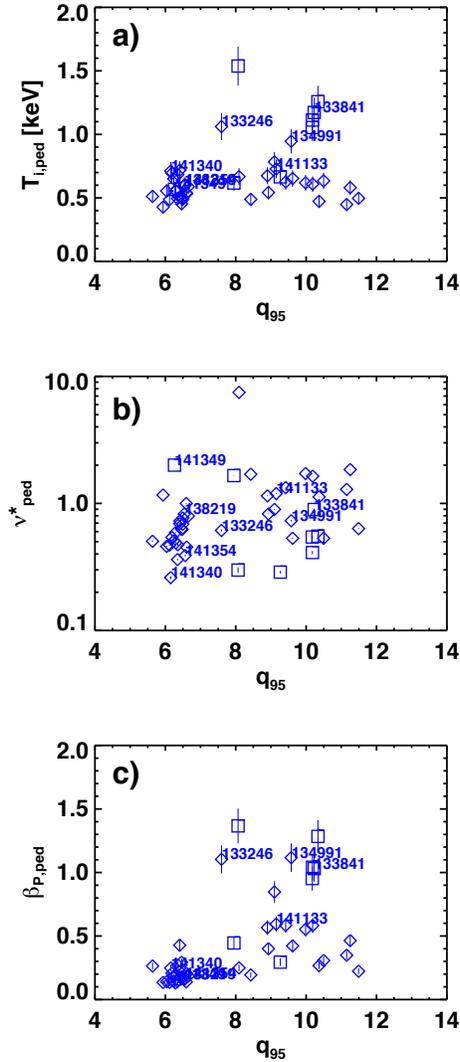
Fig. 11: a) Various quantities vs. q₉₅ for NSTX EP H-modes. Shown are a) the temperature at the top of the ion temperature pedestal, b) the pedestal top collisionality, and c) the pedestal βₚ.

4.2 Relationship between the ion temperature gradient and edge rotation

A previous publication [33] has shown that the pedestal top ion temperature is proportional to the gradient of the toroidal rotation frequency in EP H-mode. That database consisted of a small number of discharges, all of which had the steep gradient region at or quite near the separatrix. This study has been extended here to a much larger group of discharges, including those with the steep ion temperature gradient locations shifted inward from the separatrix as in Fig. 8.
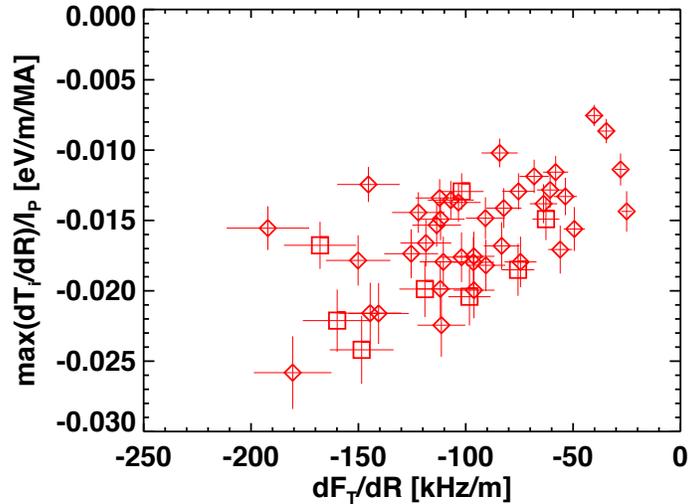
Fig. 12: The maximum ion temperature gradient, normalized to the plasma current, plotted against the radial gradient in the toroidal rotation frequency. Diamonds are for EP H-mode configurations as in Fig. 5a) and d), and squares are for configurations as Fig. 5g)

As part of this analysis, many different pedestal parameters and rotation metrics were considered, in order to find quantities with the best correlation. With regard to the pedestal performance, both the pedestal height from tanh fits and the maximum ion temperature gradient were considered, and both were taken as the direct value or normalized to the plasma current. One measure of the rotation gradient was taken as the gradient of the rotation frequency (F_T) on the small-R side of the rotation minima. Other measures include the rotation difference between the top and the bottom of the T_i pedestal, or the local value of dE_R/dR.

All combinations of these parameters were plotted, and the plot with the best correlation is shown in Fig. 12. The vertical axis here is the maximum T_i gradient, normalized by the plasma current. The gradient turns out to be a better indicator of the EP H-mode strength than the pedestal top temperature, due to cases like in Fig. 8, where the steep gradient region is shifted in, resulting in a significant vertical offset. The normalization by I_P improves the correlation by a small amount, and is roughly consistent with the EP H-mode confinement scaling with I_P, though it does not present a conclusive proof of this dependence. The horizontal axis is the simple rotation frequency gradient, as measured on the small-R side of the rotation minima. With this parameter choice, there is a clear correlation between the ion thermal transport and the rotation dynamics. Note especially that the cases with the T_i gradient shifted inwards (indicated with squares) fall in with the cases where the T_i gradient is located much closer to the separatrix, implying that the physics elements may be common.

5. Turbulence and Transport in EP H-mode

5.1 Observations of Turbulence Changes Across the H-mode-> EP H-mode transition.

As part of the present EP H-mode studies, an effort was made to examine turbulent fluctuations, to determine if they were reduced during the EP H-mode phase. The primary tool for this study was the Beam Emission Spectroscopy (BES) system [64,65]. Unfortunately, this diagnostic was available for only a subset of the discharges in this data set. The results of this study are shown in Fig. 13. Note that the frequency axes are cut off at 100 kHz, as these are the appropriate limits for ion-scale turbulence in the NSTX pedestal [66,67]. The BES spectra at higher frequencies have been examined, but do not contain any additional information. The top frame in each column also shows the plasma current (yellow) and stored energy (cyan). In each case, the data is shown from the BES chord that intercepts the neutral beam in the steep T_i gradient region; this can be verified by comparing the BES tangency radii given in the top row of Fig. 13 to the corresponding profiles shown elsewhere in this paper (see the figure captions). However, adjacent BES chords were also inspected, with similar results to those shown here. The vertical lines in the top frame bracket the time windows for the spectrograms in the lower frames. Note that due to the larger discharge duration in the left hand column and the narrow times under consideration (10 ms windows), the bracketing lines appear to blend into a single time for this discharge, while they are distinct for the discharges in the center and right column.

The left hand column shows BES data for the long pulse example in Fig. 3 & 7. Spectrograms are plotted for four different times in Fig 13b), with the red times corresponding to the H-mode phase, and the blue and cyan times corresponding to the sustained EP H-mode phase. The green spectrogram is during a short-lived EP H-mode phase. There is no clear sign of a reduction in turbulence during these EP H-mode phases; indeed, one might argue that there is a small increase in density fluctuations during the EP H-mode phase. Note also that there are no clear MHD or turbulent modes located in the pedestal in this EP H-mode example, in contrast to the Edge Harmonic Oscillation (EHO) [68] in QH-mode [68-72], the quasi-coherent mode [73,74] in enhanced D_α (EDA) H-mode [75], or the weakly coherent mode (WCM) [76] in I-mode [77,78].

The central column of Fig. 13 shows the spectra from a discharge that has a short EP H-mode phase, proceeded by and followed by H-mode phases; this discharge will be discussed in Section 6. The only spectra from the EP H-mode phase is shown in green, and the fluctuation amplitudes are found to be similar to those in the H-mode phase immediately following the transition back to H-mode (blue spectra). However, the fluctuations in the H-mode phase before the EP H-mode transition (red) and in the later H-mode phase (cyan) are significantly lower.

The right column of Fig. 13 shows the spectra for a typical "early transition" EP H-mode case. The corresponding profiles for this case are shown in Fig. 14, with the typical region of sharp T_i gradient apparent at t=0.365 s, along with a clear minima in the toroidal rotation profile. Two spectra in Fig. 13f) (red and green) are taken from the H-mode phase, and two (cyan and blue) from the EP H-mode phase. As with the other cases, the fluctuation amplitude in EP H-mode is comparable to or possibly larger than in the H-mode phase. This case also shows some residual low-n kink/tearing activity during the EP H-mode phase. This activity is common during the early phase of NSTX discharges [79], and is observed in other early EP H-mode examples. However, as noted above, it is in no way a requirement for access to EP H-mode.
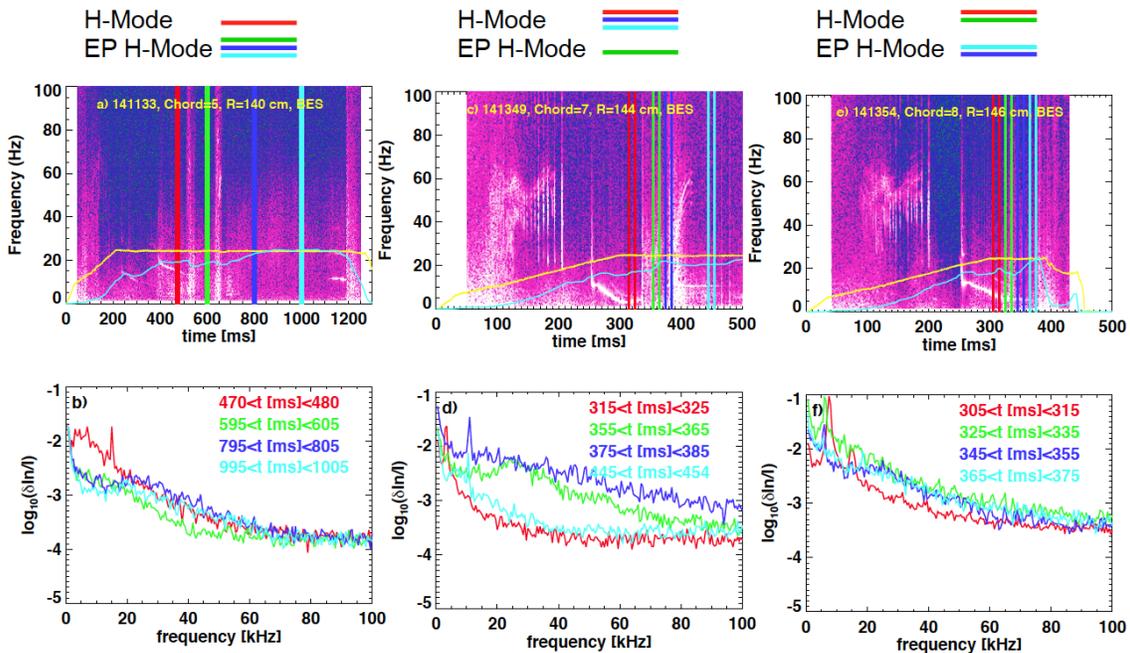
Fig. 13: Spectrograms of the BES data for three different discharges. The data in a) and b) correspond to the discharge in Figs. 3 & 7. The data in c) and d) correspond to the discharge in Fig. 18. The data in e) and f) correspond to the discharge in Fig. 14. Figs 7, 14, and 18 have vertical green lines indicating the spatial locations of the measurements. The legend above each column indicates which time slices are in H-mode and which are in EP H-mode.
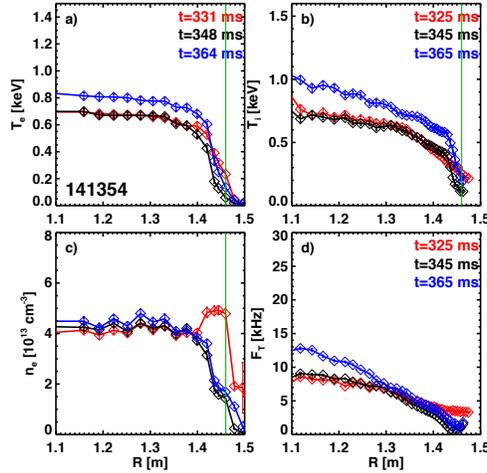
Fig. 14: Profile evolution for the EP H-mode example in Fig. 13 e) and f).

These studies were also extended to other diagnostics with sufficient bandwidth to potentially observe changes in the fluctuation behavior. No clear changes in the line averaged density fluctuations were found, as measured by the FIReTIP interferometer. In some cases, the edge magnetic fluctuations as assessed by Mirnov coils on the vessel wall appeared to show some small increase in amplitude following the EP H-mode transition. However, this was not a ubiquitous result. We also note that there was a small reduction in the poloidal correlation length (as measured by BES) in the EP H-mode phase, compared to the H-mode phase of the same discharge. Hence, it was not possible to measure any general reduction in fluctuations across the H- to EP H-mode transition in any of the fluctuation diagnostics, though there were signs that the turbulence may have some different characteristics. This will be the subject of future experiments and analysis.

5.2 Linear Microstability Analysis

The gyrokinetic stability of the EP H-mode discharge in Figs. 2 and 6 (141340) has been analyzed using the GS2 code [80]. This is an early-transition example with a particularly steep ion temperature gradient. Kinetically constrained MHD equilibria are used in these calculations, along with the fitted edge profiles used to generate these reconstructions. Three kinetic species are included—deuterium and carbon ions along with electrons—and the simulations are fully electromagnetic and include pitch-angle scattering collisions. Initial efforts focused on grid resolution checks at several edge radii to ensure the solutions are converged. Spectra of the growth rate and real frequency are shown in Figure 15 for four edge radii roughly spanning the EP H-mode pedestal. The real frequency along with eigenfunction structure (not shown) indicate that modes similar to trapped electron modes (TEM) are dominant throughout the pedestal, with the exception of a mode propagating in the ion diamagnetic direction at higher k_y at the outermost radii. The growth rates increase with radius, and over much of the pedestal are larger than the ExB shear rate (here, the ExB shear rate is a typical value for $0.8<\psi_N<0.98$, and is indicated by

the dashed horizontal line). At radii further in than shown here (ψ_N=0.7 and 0.75), modes in the wavenumber range considered are stable.

The scaling of the frequency with various parameters such as gradient scale lengths and β have been calculated for a radius of ψ_N=0.90 (roughly at the mid-pedestal). These scans have been performed two ways: 1) by varying gradient scale lengths only, while leaving the magnetic geometry fixed, and 2) by using a local MHD equilibrium model to change the pressure gradient within the magnetic geometry and keeping it consistent with the (varying) parameters during scans. This is an important difference, since increasing the pressure gradient in the MHD equilibrium tends to be strongly stabilizing, and can partially or even fully offset the destabilizing effect of increasing (for example) the temperature gradient. In Fig. 16, results using the first method (single parameters varied individually) are shown as the red curves, while those using the second method (geometry recalculated using a pressure gradient consistent with the other parameters at each point in a scan) are shown in black.
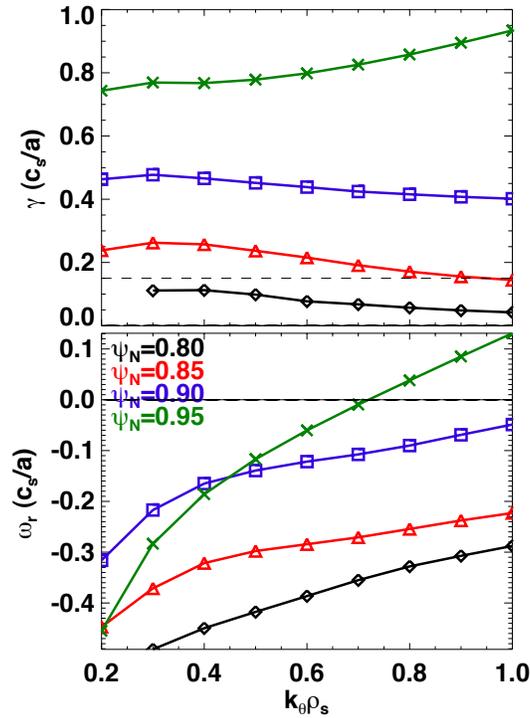
Fig. 15: Spectra of the growth rate (top) and real frequency (bottom) for TEM-like modes in the EP H-mode pedestal. The different colors correspond to different radial locations.

As the figure shows, if the geometry is held fixed, increasing any one of β, the density gradient, or the electron and ion temperature gradients by less than a factor of two causes a kinetic ballooning mode (KBM) to become destabilized (as evidenced by a sharp increase in the growth rate and a strongly positive real frequency). However, with a consistent MHD equilibrium calculated at each point,

KBM onset is never observed. This is consistent with the plasma being in the second-stable regime, which has been verified through calculations of ideal ballooning stability. At the nominal parameters (vertical dashed line), increasing the electron temperature gradient has the strongest destabilizing effect. The density gradient is weakly stabilizing, with microtearing modes appearing at very low values of a/L_{ne} (evidenced by the transition to large magnitude negative real frequency). Increasing the ion temperature gradient is strongly stabilizing, regardless of how the geometry is treated (aside from the transition to KBM). This suggests that the increased ion temperature gradient measured in the EP H-mode does not lead to degraded microstability, and may be consistent with the dominance of neoclassical transport in the ion channel. Overall, the dependences found here are reasonably consistent with the dominant mode being a TEM/KBM hybrid mode as found in pedestal calculations during standard and lithiated H-modes [81] with a smooth transition between negative and positive real frequency as the KBM threshold is approached (in the case where the geometry is held fixed). One difference, however, is the β dependence found here, where increasing β is stabilizing near the nominal value even in the case where the geometry is not changed.
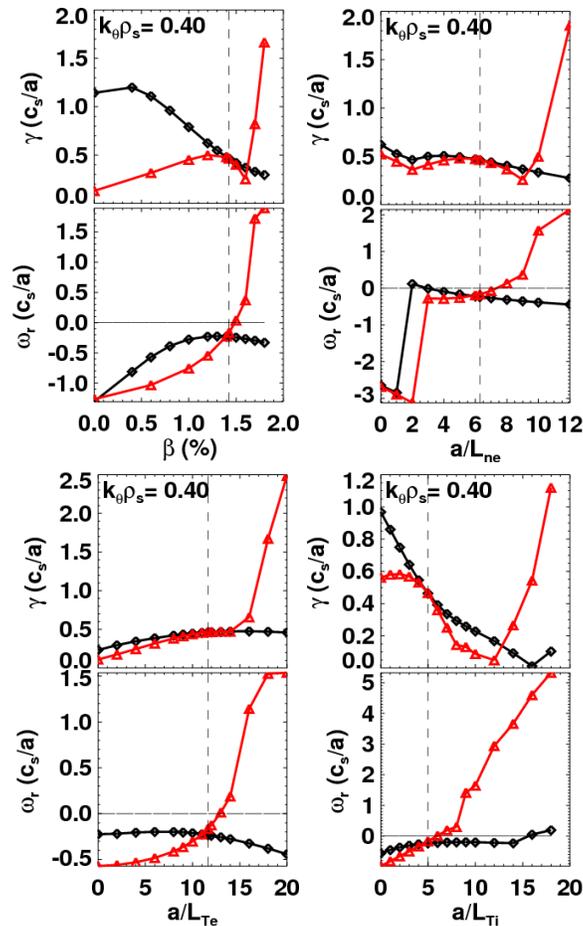
Fig. 16: Growth rate and real frequency of the dominant instabilities in the example EP H-mode pedestal, as a function of (upper left) β, (upper right) the density gradient, (lower left)

5.3 Comparison of the ion transport to neoclassical theory.

As indicated above, both the lack of turbulence changes following the EP H-mode transition and the microstability calculations lead one to question if the EP H-mode T_i profile dynamics are determined by neoclassical physics. In order to make a first test of this hypothesis, the ion temperature profiles for the discharges 134991 (Fig. 3 and 5), 141340 (Figs. 2 and 5, and 6), and 133841 (Figs 5 and 8) have been compared to the results of neoclassical predictions. In particular, the neutral beam heating parameters, electron, ion and impurity density profiles, and electron temperature profiles were used as inputs to the TRANSP code. The ion temperature profile was predicted using the Chang-Hinton model [82] for the neoclassical thermal diffusivities, and no model for anomalous (turbulent) ion heat transport was used.
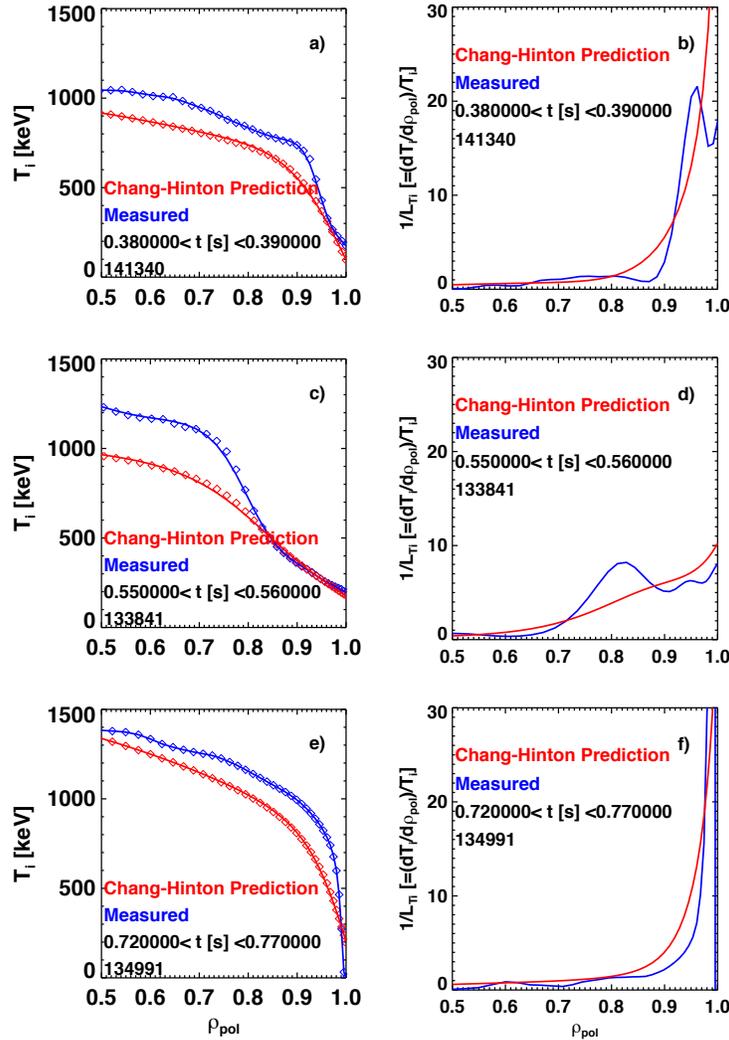
Fig. 17: Ion temperature profiles (left column) and inverse T_i gradient scale lengths (right column) during the EP H-mode phase of three discharges. The red curves are from predictions

The results from this analysis are shown in Fig. 17. The left frame shows the mapped T_i profiles, where the radial coordinate ρ_{pol} is defined as the square root of the normalized poloidal flux. The measured profile is shown in blue, while the prediction from the Chang-Hinton model is given in red. The symbols are the values determined by the TRANSP mapping routines. The solid lines are spline fits to these profiles. These spline fits are then used to determine the inverse scale lengths $(1/L_{Ti})$ shown in the right column, calculated from $L_{Ti}=T_i/(dT_i/d\rho_{pol})$.

For discharge 141340 in the top row, the region of steep T_i is at $\rho_{pol}\sim0.92$, and frame a) shows that the T_i gradient is comparable or exceeds that predicted by neoclassical predictions; this is visible in either the raw profiles, or the higher values of $1/L_{Ti}$ in frame b). Discharge 133841 in the middle row is an example of a case where the region of steep T_i gradient is shifted inwards. In this case, the local gradient clearly exceeds that predicted by this simple neoclassical model. Finally, discharge 134991 in the bottom row has the steep gradient region at the very edge of the plasma. Once again, the T_i gradient appears steeper than predicted by the simple neoclassical model.

It should be noted that this analysis does not indicate that neoclassical theory is violated, as the Chang-Hinton model is a purely local model, based on assumptions that are typically violated in these plasmas. The values of χ_i have been evaluated with NCLASS [83] and NEO [84] and compared to the predictions from the Chang-Hinton model. They generally show ion thermal diffusivities a factor of 2-3 lower than the Chang-Hinton model in the region of the steep temperature gradient, which would result in a steeper ion temperature gradient. In order to fully understand this physics, these EP H-mode cases are being evaluated with the full-f Monte Carlo code XGC0 [85]. The results of this analysis will be presented in a future publication.

6. Control of the EP H-mode Transition

The examples in Sect. 2 show that EP H-modes can be sustained for multiple confinement times in near-stationary conditions. However, to fully exploit this regime, mechanisms to better control the onset and sustainment of the EP H-mode phase must be developed. This section will explore various means of triggering EP H-modes

6.1 Natural Onset in Low q_{95} discharges

A first method for routinely generating EP H-mode discharges is to determine a plasma scenario where the plasma naturally transitions to this regime at a reliable and repeatable time. Based on operational experience, it was known that low q_{95} discharges often had those characteristics, with an early ELM that often triggered a

transition to EP H-mode. Hence, this configuration was chosen for a dedicated experiment.

In this experiment, a series of 22 high current (I_P=1200 kA) discharges were formed; discharge 141340 from Figs. 2, 5, 6, 16 and 17 was part of this sequence. The first EPH transition occurred in the 3rd discharge, and in 13 of the following 19 discharges. This indicated that, under the right circumstances, these transitions could be fairly reliable. The experimental plan was then to use β_N-control [15,86] to limit the growth of the pressure and avoid the disruption.

A representative discharge from this sequence is shown in Fig 18. The discharge transitions to EP H-mode following the ELM at t=0.34 s, and there is a rapid increase in the stored energy. A region of steep ion temperature also forms, as visible in the t=0.365 s profiles in Fig. 18b), and a local minima in the rotation frequency profile is visible. The neutral beam power is then rapidly ramped down by the β_N controller. However, a second ELM at t=0.380 s causes the plasma to fall out of EP H-mode, and the discharge continues on in traditional H-mode. Note that this and similar H-mode discharges, operating at high current and low power, produced some of the highest absolute confinement times observed in NSTX H-modes, with $\tau_{E,th}$>=80 ms.

Hence, while this experiment showed the ability to generate this configuration reliably, it was not possible to maintain the configuration. This underscores the importance of better understanding the macrostability of the edge pedestal [87] in these cases, likely using codes such as ELITE [88,89] which have proven successful in understanding [53,60] the suppression of ELMs with lithium PFC conditioning [90] in NSTX. Experimentally, repeating these experiments with heavier lithium conditioning of the PFCs may help delay or eliminate ELMs, if the stability of the EP H-mode pedestal is modified in a way similar to the H-mode modifications [53,60].
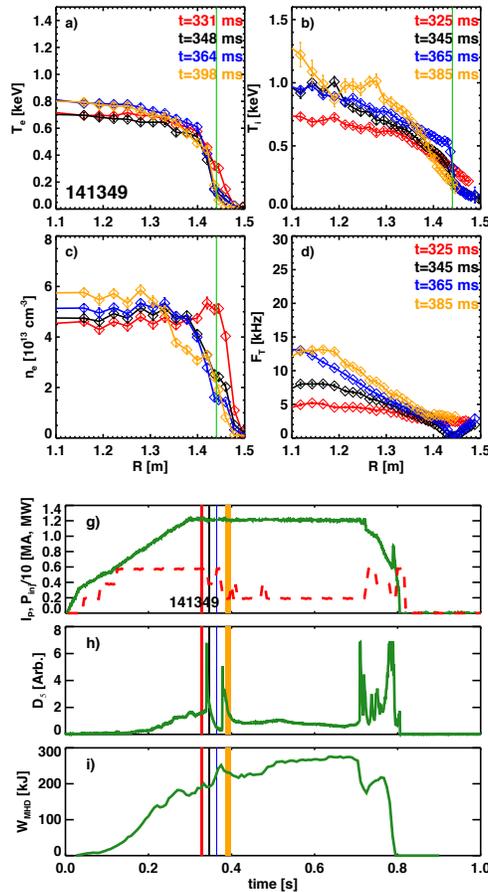
Fig. 18: Profile evolution and time traces from a discharge that transitions into and out of EP H-mode. The quantities shown are the same as in Fig. 6. The plasma is in the EP H-mode state for the middle two times in the profile figures. See text for additional details.

6.2 EP H-mode Transitions Driven by Triggered ELMs

A second means of generating EP H-modes may be to deliberately trigger an ELM, which leads to EP H-mode. ELM triggering has been observed in NSTX via vertical jogs [91] and 3D field application [56-28]. Injection of small pellets has also demonstrated ELM triggering in many tokamaks [92-98]. Fig. 19 illustrates a case where a series of pulsed 3D fields are used to generate a sequence of triggered ELMs. This is best illustrated in frame b) where the small transients in the RWM coil current (black) are each followed by an ELM (the small DC offset in the RWM coil current is for n=3 error field correction [99], while the applied 3D fields also are n=3). The final triggering pulse is at t= 0.85 s, and the associated ELM triggers a transition to EP H-mode. The subsequent confinement increase achieves $H_{98(y,2)}$=1.3 before the plasma disrupts. Note that this example comes from an experiment designed to study ELM pacing, not EP H-mode transitions. Also recall that the EP H-mode example discussed in Fig. 8 was initiated by an externally triggered ELM.
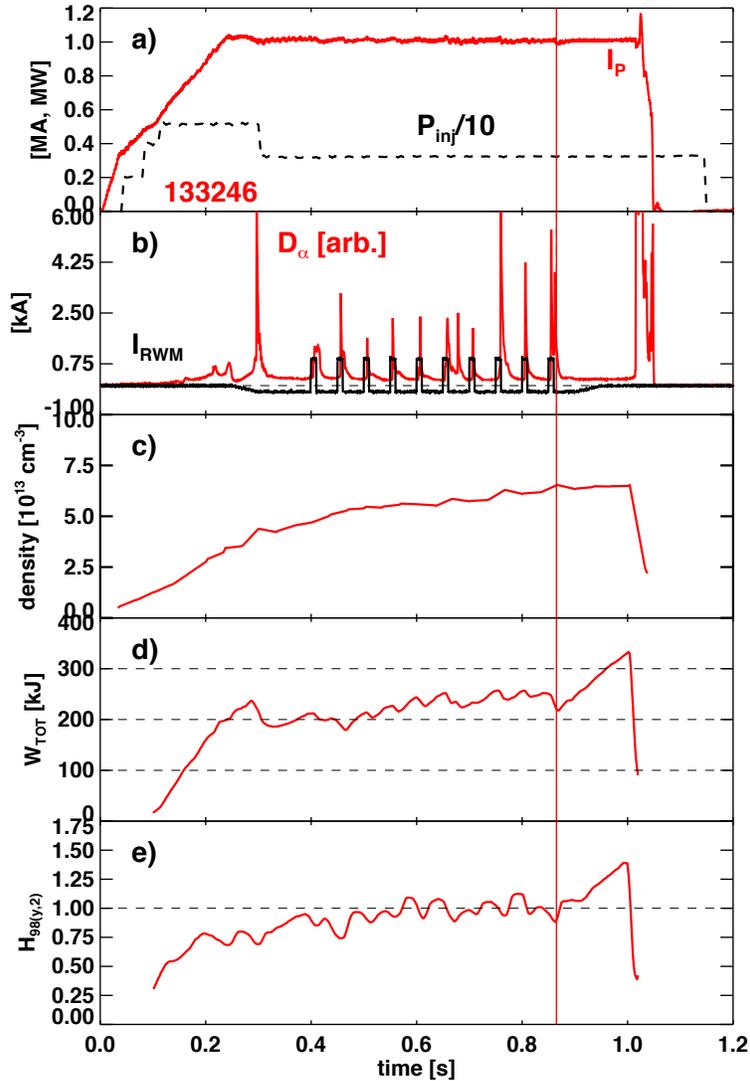
Fig. 19: Example of EP H-mode configuration initiated by a triggered ELM. Shown are a) the plasma current and injected power, b) divertor D_α and RWM coil current, c) line-averaged density, d) stored energy, and e) $H_{98(y,2)}$ confinement multiplier. The vertical line indicates the time of the EP H-mode transition.

Motivated by this and other examples, an experiment was done to trigger EP H-mode transitions via pulsed fields. In that experiment, lower current ($900 < I_P$ [kA] < 1000) discharges were selected. Lithium conditioning of the PFCs was used, as was super sonic gas injection (SGI), motivated by the use of that fuelling technique for discharge 134991 (see Section 2.1). However, despite trying a range of fuelling methods and trigger pulses, it was not possible to generate the EP H-mode configuration via triggered ELMs in this first dedicated experiment. Two discharges from this experiment spontaneously transitioned to EP H-mode before the first externally triggered ELM, and those two discharges are included in the database analysis described above. Hence, while the data like in Fig. 18 show that it is possible to trigger this configuration with externally triggered ELMs, it is clear that

additional characteristics of the discharge play a role. Identifying those characteristics will be a topic of research on NSTX-Upgrade.

7. Summary

This paper has documented many features of the enhanced pedestal (EP) H-mode in NSTX. Key findings include:

- While many examples of EP H-modes are short lived, examples exist of longer-pulse EP H-modes of several confinement time duration, including a recently observed very quiescent case (Section 2).
- The location of the steep T_i gradient can be either directly at the separatrix, or shifted in a considerable distance. Indeed, the latter cases appear more like discharges with a large-radius internal transport barrier (Section 3).
- The largest component of the energy increase following the EP H-mode transition is in the ion channel. Confinement multipliers up to $H_{98(y,2)} \sim 2$ have been observed (Section 4).
- The EP H-mode regime has been observed over a range of collisionalities and q_{95} (Section 4).
- The steepness of the ion temperature gradient in EP H-mode is correlated with the local gradient in the toroidal rotation frequency shear (Section 4).
- No significant changes in the measured fluctuation characteristics in EP H-mode have been observed, compared to similar H-modes (Section 5).
- Microstability calculations and neoclassical transport have been initiated. While some microturbulent modes are linearly unstable, the analysis indicates that the ion thermal transport is at or beneath the neoclassical level projected by a simple local model. (Section 5).
- Experiments designed to reliably form and sustain EP H-mode plasmas have met with mixed success. An experiment to sustain low-q_{95} EP H-modes was quite successful in generating the configuration, but maintaining the configuration was difficult. While examples exist of externally triggered ELMs resulting in a transition to EP H-mode, a first experiment dedicated to reproducing this effect proved unsuccessful (Section 6).

It is interesting to compare this confinement regime to the VH-mode [22-28] observed at JET and DIII-D. VH-mode was first observed with boronization of the DIII-D vacuum chamber [22], though examples without a recent boronization were subsequently observed [26]. The EP H-mode in NSTX was observed before lithium conditioning of the PFCs was common, but the frequency of occurrence has increased with more regular use of lithium as a plasma facing component; the two examples of sustained EP H-modes shown in Fig. 3 both used Li conditioning of the PFCs. The VH-mode is characterized by edge transport barriers that are broader than in H-mode, which is also somewhat similar to the rather broad edge localized barriers seen in EP H-mode (see Figs. 7 and 8, for example). However, VH-mode is

generally facilitated by the increase in toroidal rotation in the region just inside the pedestal. This is referred to at the "spin-up" in Ref. [26], and this increase in rotation and rotation shear is though to result in a broader region of ExB shear and associated turbulence suppression [26,27]. In contrast, the EP H-mode is often formed by a localized decrease in toroidal rotation towards the edge, which results in a region of increased rotation shear. Hence, while a region of broad toroidal flow shear may be important for both configurations, the mechanisms by which that flow shear is generated are significantly different. Finally, a key element in achieving high-quality VH-modes was the avoidance of the first ELM following the L-H transition. Ref. [26] shows how the experimental actuators that delay the first ELM also result in higher VH-mode performance. In contrast, the EP H-mode is often triggered by an ELM (often the first large ELM following the L->H transition, as in Figs. 2 & 6). Hence, while the two regimes share some similarities, there are also many significant differences.

The work presented in this paper represents only an initial assessment of the physics elements of the EP H-mode configuration, with many additional steps yet to be completed.

On the analysis side, it is necessary to better understand numerous physics aspects of these configurations. One key issue is to better understand the peeling-ballooning stability of the configuration. As was indicated in Section 6, ELMs during the EP H-mode phase often drive a transition back to H-mode. However, the data in Figs. 3 & 7 show a case where an ELM occurs during EP H-mode, yet the configuration recovers into EP H-mode again. Due to the large pedestal pressures in these cases, ELMs during EP H-mode would likely be particularly large, with numerous detrimental aspects in a burning plasma configuration. Luckily, examples such as in Fig. 3 & 7 show long periods in the EP H-mode configuration, without any ELMs. It is likely that the heavy lithium coatings used in these examples assisted in the suppression of these ELMs. A complete assessment of this physics will require numerous peeling-ballooning stability calculations based on kinetic EFITs, a task that has only recently been initiated.

A second key analysis task is to complete a more thorough neoclassical analysis of the ion transport, using the code XGC0, including comparisons to similar H-mode discharges. A single XGC0 analysis of a time slice in discharge 141133 showed that the ion temperature profile could be reproduced using the purely neoclassical transport, but detailed comparisons of the XGC0 results to H-mode examples or simpler neoclassical models have not been executed.

It is also necessary to better understand the microstability characteristics of these discharges. The data in Section 5 indicates that turbulent modes are linearly unstable, but that the transport level remains at the neoclassical levels during the EP H-mode phase. Indeed, the observed reduction of the growth rates with increasing T_i gradient may be speculated to provide a bootstrapping effect, where the increased gradient results in reduced turbulent transport. This topic must be

revisited with full-physics non-linear turbulence simulations, a challenging task outside the scope of this study.

Experimentally, the key task is to develop better methods to trigger and sustain the EP H-mode configuration.

With regard to triggering, it is necessary to better understand how ELMs trigger a transition to EP H-mode. The data in Fig. 6 indicate that immediate loss of edge pressure following an ELM leads to a small region of steep gradient T_i, which they increases in width at fixed gradient; a key variable in this case may be the radial width of the zone eroded by the ELM, although systematic studies along these lines have not been attempted. This explanation by itself does not, however, explain the sustained local minima in the rotation profile. As discussed above in Section 3.2 and below, there has been speculation that the local minimum is due to torque from a magnetic island at this location, though assessing this physics in detail has proven challenging. This remains a topic of future work.

While spontaneously transitioning EP H-modes appeared repeatable once the discharge scenario was established, further work is required to *sustain* these scenarios. Heavy lithium conditioning of the PFCs appears to be a plausible means of avoiding ELMs in EP H-mode, provided that it does not prevent the first ELM which drives the EP H-mode transition. If that ELM is suppressed, then externally triggering of the EP H-mode transition appears to be necessary. Further work is required in order to understand the conditions where triggered ELMs actually lead to an EP H-mode transition.

Finally, the potential role of 3D distortions during EP H-mode must be addressed. As can be inferred from the profiles in Fig. 5, the electron temperature profile is shifted inward compared to the ion temperature profile during the EP H-mode phase. These profiles typically line up well in H-mode, increasing confidence in the spatial calibrations of these diagnostics. However, the diagnostics are toroidally separated by ~180°, and it is thus possible that the profile shift in EP H-mode is indicative of a 3D distortion. If this were so, the interpretation of the MSE data would also be more complicated and the 2D equilibrium reconstructions used to generate the q-profiles in Figs. 6-8 would be called into question. On the other hand, the quality of the 2D equilibrium reconstruction, as measured by the goodness of fit parameter χ^2, does not degrade following the transition to EP H-mode, and the observed displacements between T_e and T_i appear to be independent of the configuration of the known error field sources in NSTX. These latter two considerations appear to imply that the EP H-mode plasma can be understood using 2D axisymmetric equilibria and transport physics, an assumption that has been used for all analysis in this paper.

Overall, this research shows the potential benefits of the EP H-mode configuration for next step STs, while also illuminating both the transport-physics and practical

triggering and sustainment uncertainties associated with the configuration. Research to better understand the critical transport physics is ongoing. The experimental aspects of these studies will be continued when NSTX-U [100] commences operation, providing access to regimes with higher field and current, higher hearing power, and lower collisionality [101].

8. Acknowledgements

Appendix: Database of EP H-mode TRANSP runs and Equilibrium Reconstructions

As part of this study, a database of EP H-mode analysis was created using the codes LRDFIT and TRANSP. A subset of data relevant from this database are shown in Table A1. Note that EP H-mode type 0 corresponds to those cases with the steep gradients near the separatrix (diamonds in the scatter plots above), while the type 1 EP H-modes correspond to cases with the T_i gradient shifted inwards (squares in the scatter plots above). The $H_{98(y,2)}$ values are those from Fig. 10b). "eindex" indicates the specific execution of the LRDFIT code used in the database analysis.

Shot	H-mode Time [s]	EP H-mode Time [s]	I_P [kA]	B_T [T]	q_{95}	$H_{98(y,2)}$ in EP H-mode	EP H-mode Type	eindex	TRANSP ID
129268	0.53	0.64	894	-0.44	9.4	1.3	0	-7	B01
133246	0.865	1	986	-0.44	7.6	1.5	0	-7	A04
133841	0.43	0.56	794	-0.44	10.2	1.2	1	-9	B09
133851	0.42	0.526	794	-0.44	10.3	1.1	1	-9	B06
134970	0.25	0.27	894	-0.47	9.3	1.1	1	-9	B06
134987	0.89	0.98	871	-0.47	9.2	1.6	0	-7	B04
134991	0.5	0.725	888	-0.47	9.6	2.0	0	-4	A22
135192	0.5	0.69	795	-0.44	10.2	1.0	1	-7	B01
138169	0.25	0.32	910	-0.44	9.6	1.0	0	-4	A02
138173	0.23	0.32	968	-0.44	8.6	1.0	0	-4	A02
138216	0.31	0.36	1205	-0.44	6.4	1.0	0	-12	A28
138217	0.34	0.37	1212	-0.44	6.7	0.8	0	-10	A06
138219	0.33	0.36	1202	-0.44	6.5	1.1	0	-10	A21
138222	0.31	0.35	1217	-0.44	6.6	0.8	0	-10	A17
138226	0.28	0.32	1141	-0.44	6.5	0.7	0	-10	A14
138522	0.25	0.3	1056	-0.44	6.1	0.7	0	-10	A05
138524	0.255	0.28	1063	-0.44	6.0	0.7	0	-10	A04
138532	0.315	0.33	1271	-0.44	5.9	0.6	0	-10	A02
138540	0.3	0.328	1212	-0.45	6.3	0.6	0	-10	A03
139016	0.3	0.335	701	-0.49	11.2	1.3	0	-10	A03
139281	0.3	0.335	1205	-0.39	5.6	0.8	0	-10	A09
139349	0.4	0.55	1009	-0.44	7.9	0.9	1	-9	B05
139605	0.23	0.266	885	-0.47	11.5	1.3	0	-12	A07
139771	0.24	0.275	903	-0.47	8.9	1.2	0	-9	A06
139905	0.715	0.795	887	-0.47	7.4	1.4	1	-12	A05
139913	0.445	0.515	862	-0.47	8.1	1.3	1	-12	A02
139958	0.63	0.72	904	-0.44	8.9	1.5	0	-12	A06
140108	0.38	0.4	1105	-0.49	8.4	0.8	0	-12	B06
140161	0.38	0.48	806	-0.44	10.2	1.3	1	-9	B03
141133	0.65	0.85	896	-0.44	9.1	1.5	0	-7	B11
141146	0.675	0.84	991	-0.44	8.1	1.2	0	-12	B02
141177	0.49	0.555	891	-0.44	10.2	1.2	0	-7	B04
141186	0.92	0.98	901	-0.44	9.1	1.4	0	-9	B04
141187	0.35	0.585	903	-0.44	10.0	1.3	0	-12	B08
141337	0.34	0.385	1209	-0.44	6.2	0.9	0	-12	B18
141338	0.31	0.35	1201	-0.44	6.5	0.7	0	-12	B09
141339	0.3	0.375	1208	-0.44	6.4	0.7	0	-12	B05
141340	0.32	0.39	1215	-0.44	6.2	0.8	0	-12	B04
141343	0.34	0.365	1207	-0.44	6.3	0.8	0	-12	B04
141344	0.31	0.35	1206	-0.44	6.5	0.7	0	-12	B07
141345	0.305	0.365	1208	-0.44	6.4	0.7	0	-12	B09
141346	0.33	0.375	1213	-0.44	6.2	1.0	0	-7	B17
141347	0.335	0.365	1211	-0.44	6.3	0.7	0	-12	B05
141348	0.31	0.35	1207	-0.44	6.5	0.7	0	-12	B06
141349	0.34	0.375	1210	-0.44	6.3	0.7	1	-12	B05
141353	0.34	0.366	1201	-0.44	6.6	0.8	0	-12	B13
141354	0.34	0.375	1203	-0.44	6.6	0.9	0	-12	B03
141454	0.25	0.33	894	-0.44	10.5	1.1	0	-7	B05
141476	0.38	0.58	818	-0.44	11.3	0.9	0	-9	B06
141761	0.2	0.265	846	-0.54	10.4	0.7	0	-9	B04
141768	0.2	0.32	846	-0.54	9.6	0.9	0	-9	B04
142185	0.2	0.28	925	-0.54	10.0	1.0	0	-9	B06

Table A1: TRANSP and LRDFIT runs used in this analysis, as well as the times of interest for the various discharges.

References

[1] Y.K.M. Peng and D.J. Strickler, Nuclear Fusion **26** (1986) 769.
[2] Y-K M Peng, et al., Plasma Phys. Control. Fusion **47** (2005) B263.
[3] G.M. Voss, et al., Fusion Eng. and Design **83**, 1648 (2008).

[4] Y-K M Peng, et al., *Effects of Physics Conservatism and Aspect Ratio on Remote Handling for Compact Component Test Facilities (CTFs)*, Paper FT/P3-14, Geneva (2008).
[5] Y-K M Peng, et al, Fusion Science and Technology **56**, 957 (2009).
[6] R.D. Stambaugh, et al., *Candidates for a Fusion Nuclear Science Facility (FDF and ST-CTF),* Paper P2.110, 37th EPS Conference on Plasma Physics, Dublin, Ireland (2010).
[7] J. E. Menard, et al., Nuclear Fusion **51**, 103014 (2011).
[8] F. Najmabadi and the ARIES Team, Fusion Eng. And Design **65**, 143 (2003).
[9] H.R. Wilson, et al., Nuclear Fusion **44**, 917 (2004).
[10] ITER Physics Experts Groups, Nuclear Fusion **39** (1999) 2175.
[11] M. Abdou, Fusion Eng. And Design **27**, 111 (1995).
[12] S.M. Kaye, et al., Plasma Phys. Control. Fusion **48,** A429 (2006).
[13] S.M. Kaye, et al., Nuclear Fusion **46**, 848 (2006).
[14] S.M. Kaye, et al., Nuclear Fusion **47**, 2007 (499)
[15] M. Valovic, et al., Nuclear Fusion **49**, 075016 (2009).
[16] S.P. Gerhardt, et al., Nuclear Fusion **51**, 073031 (2011).
[17] H. Kugel, et al., Phys. Plasmas **15**, 056118 (2008).
[18] M.G. Bell, et al, Plasma Phys. Control. Fusion **51**, 12 (2009).
[19] S. Ding, et al., Plasma Phys. Control. Fusion **52**, 015001 (2010).
[20] R. Maingi, et al., Phys. Rev. Lett. **107**, 145005 (2011).
[21] R.C. Wolf, Plasma Phys. Control. Fusion **45**, R1 (2003).
[22] G.L. Jackson, et al., Phys. Rev. Lett. **67**, 3098 (1991).
[23] C.M. Greenfield, et al., Plasma Phys. Control. Fusion **35**, B263 (1993).
[24] T.H. Osborne, et al., Plasma Phys. Control. Fusion **36**, A237 (1994).
[25] N. Deliyanakis, et al., Plasma Phys. Control. Fusion **36**, 1159 (1994).
[26] T.H. Osborne, et al., Nuclear Fusion **35**, 23 (1995).
[27] R. J. La Haye, et al., Nuclear Fusion **35**, 988 (1995).
[28] G.L. Jackson, et al., Phys. Plasmas **3**, 1005 (1996).
[29] H. Yuh, et al., Phys. Plasmas **16**, 056120 (2009).
[30] H. Yuh, et al., Phys. Rev. Lett. **106**, 055003 (2011).
[31] J.R. Wilson, et al., Phys. Plasmas **10**, 1733 (2003).
[32] R. Maingi, et al., Journal of Nuclear Materials **390-391**, 440 (2009).
[33] R. Maingi, et al., Phys. Rev. Lett. **105**, 135004 (2010).
[34] M. Ono, et al. Nuclear Fusion **40**, 557 (2000).
[35] T. Stevenson, et al., A neutral beam injector upgrade for NSTX, PPPL Report 3651 (2002).
[36] B.P. LeBlanc, et al., Rev. Sci. Instrum. **74**, 1659 (2003).
[37] R.E. Bell and R. Feder, Rev. Sci. Instrum. **81**, 10D724 (2010).
[38] F. Levinton and H. Yuh, Rev. Sci. Instrum. 79, 10F522 (2008).
[39] J.E. Menard, et al., Phys. Rev. Lett. **97**, 095002 (2006).
[40] S.A. Sabbagh, et al., Nuclear Fusion **41**, 1601 (2001).
[41] S.A. Sabbagh, et al., Nuclear Fusion **46**, 635 (2006).
[42] L.L Lao, Nuclear Fusion **25**, 1611 (1985).

[43] R. J. Hawryluk, et al., "An Empirical Approach to Tokamak Transport", in Physics of Plasmas Close to Thermonuclear Conditions, ed. by B. Coppi, et al., (CEC, Brussels, 1980), Vol. 1, pp. 19-46.

[44] A. Pankin, et al., Comput. Phys. Commun. **159**, 157 (2004).

[45] H.W. Kugel, et al, Fusion Engineering and Design **84**, 1125 (2009).

[46] E. Kolemen, et al, Nuclear Fusion **50**, 105010 (2010).

[47] E. Kolemen, et al., Nuclear Fusion **51**, 113024 (2011).

[48] V.A. Soukhanovskii, et al., Rev. Sci. Instrum **75**, 4320 (2004).

[49] R. Maingi, et al., Plasma Phys. Control. Fusion **46**, A305 (2004).

[50] D. A. Gates, et al, Phys. Plasmas **13**, 056122 (2006).

[51] F. Scotti, et al., Nuclear Fusion **53**, 083001 (2013).

[52] D.A. Gates, at al., Nuclear Fusion **46**, 17 (2006)

[53] D. Boyle, et al., Plasma Phys. Control. Fusion **53**, 105011 (2011).

[54] C.B. Markwardt, 2009, "Non-Linear Least Squares Fitting in IDL with MPFIT," in proc. *Astronomical Data Analysis Software and Systems XVIII*, Quebec, Canada, ASP Conference Series, Vol. 411, eds. D. Bohlender, P. Dowler & D. Durand (Astronomical Society of the Pacific: San Francisco), p. 251-254 (ISBN: 978-1-58381-702-5).

[55] R.E. Bell, et al., Phys. Plasmas **17**, 082057 (2010).

[56] J. M. Canik, et al., Phys. Rev. Lett. **104**, 045001 (2010).

[57] J.M. Canik, et al., Nuclear Fusion **50**, 064016 (2010).

[58] J.M. Canik, et al., Nuclear Fusion **50**, 034012 (2010).

[59] A. Diallo, et al., Nuclear Fusion **51**, 103031 (2011).

[60] R. Maingi, et al., Phys. Rev. Lett., **103**, 075001 (2009).

[61] R. Maingi, et al., Nuclear Fusion **45**, 1066 (2005).

[62] A. Diallo, et al., Rev. Sci. Instrum. **83**, 10D532 (2012).

[63] B.P. LeBlanc, et al., Rev. Sci. Instrum. **83**, 10D527 (2012).

[64] D.R. Smith, et al., Rev. Sci. Instrum. **81**, 10D717 (2010).

[65] D.R. Smith, et al., Rev. Sci. Instrum. **83**, 10D502 (2012).

[66] D.R. Smith, et al., Physics of Plasmas **20**, 055903 (2013).

[67] D.R. Smith, et al., Nuclear Fusion **53**, 113029 (2013).

[68] K.H. Burrell, et al., Phys. Plasmas **12**, 056121 (2005).

[69] K.H. Burrell, et al., Nuclear Fusion **49**, 085024 (2009).

[70] A.M. Garofalo, et al., Nuclear Fusion **51**, 083018 (2011).

[71] K.H. Burrell, et al., Phys. Plasmas **19**, 056117 (2012).

[72] K.H. Burrell, et al., Nuclear Fusion **53**, 073038 (2013).

[73] A.E. Hubbard, et al., Phys. Plasmas **8**, 2033 (2001).

[74] J.L. Terry, et al., Nuclear Fusion **45**, 1327 (2005).

[75] M. Greenwald, et al., Phys. Plasmas **6**, 1943 (1999).

[76] A. E. Hubbard, et al., Phys. Plasmas **18**, 056115 (2011).

[77] R. McDermott, et al., Phys. Plasmas **16**, 056103 (2009).

[78] D. Whyte, et al., Nuclear Fusion **50**, 105005 (2010).

[79] S.P. Gerhardt, et al., Nuclear Fusion **53**, 043020 (2013).

[80] M. Kotschenreuther *et al*, Comput. Phys. Commun. **88** (1995) 128.

[81] J.M. Canik, et al., Nuclear Fusion **53**, 113016 (2013).

[82] C.S. Chang and F.J. Hinton, Phys. Plasmas **25**, 1493 (1982).
[83] W.A. Houlberg et al., Phys. Plasmas **4**, 9 (1997).
[84] E.A. Belli et al., Plasma Phys. Control. Fusion **50**, 095010 (2008).
[85] C.S. Chang, S. Ku, and H. Weitzner, Phys. Plasmas **11**, 2649 (2004).
[86] S.P. Gerhardt, et al., Fusion Sci. and Tech. **61**, 11 (2012).

[87] P.B. Snyder, et al., Plasma Phys. Control. Fusion **46**, A131 (2004).
[88] P.B. Snyder, et al., Phys. Plasmas **9**, 2037 (2002).
[89] H.R. Wilson, et al., Phys. Plasmas **9**, 1277 (2002).
[90] D.K. Mansfield, et al., Journal of Nuclear Materials **390-391**, 764 (2009).
[91] S.P. Gerhardt, et al., Nuclear Fusion **50**, 064015 (2010).
[92] P. T. Lang, et al, Nuclear Fusion **44**, 665 (2004).
[93] P.T. Lang, et al., Nuclear Fusion **47**, 754 (2007).
[94] P.T. Lang, et al., Nuclear Fusion **48**, 095007 (2008).
[95] P.T. Lang, et al., Nuclear Fusion **51**, 033010 (2011).
[96] L.R. Baylor, et al., Phys. Rev. Lett. **110**, 245001 (2013).
[97] P.T. Lang, et al., Nuclear Fusion **53**, 043004 (2013).
[98] D. K. Mansfield, et al., Nucl. Fusion **53**, 113023 (2013).
[99] S.P. Gerhardt, et al., Plasma Phys. Control Fusion **52**, 104003 (2010).
[100] J.E. Menard et al., Nuclear Fusion **52** 083015 (2012).
[101] S.P. Gerhardt, et al., Nuclear Fusion **52**, 083020 (2012).

Princeton Plasma Physics Laboratory
Office of Reports and Publications

Managed by
Princeton University

under contract with the
U.S. Department of Energy
(DE-AC02-09CH11466)